ORIGINAL ARTICLE

Initiation and growth of edge cracks after shear cutting of dual-phase steel

Mahdi Masoumi Khalilabad[1] · Semih Perdahcıoğlu[1] · Eisso Atzema[1,2] · Ton van den Boogaard[1]

Abstract

Dual-phase steels suffer from low edge ductility, which limits their formability. In this study, an in-plane bending test is used to investigate the initiation and evolution of edge cracks. The edges of samples were prepared by shear cutting and afterwards further deformed by the in-plane bending test. Void distribution and non-uniform plastic deformation were explored with the help of scanning electron microscope (SEM) and electron backscatter diffraction (EBSD) analysis and microhardness measurement in different regions of the material edge. The extent of micro-cracks was revealed by microcomputed tomography (μCT) scan. The result shows that the blanking process creates inhomogeneous void distribution in the thickness direction. As the deformation increases during the subsequent in-plane bending test, the micro-cracks initiate at the burr region and grow towards the rollover region. Once they entirely pass the thickness of the material, they grow further, away from the edge. High roughness, plastic deformation, and void volume fraction were observed at the burr region, triggering crack initiation. The in-plane bending test successfully distinguished the dominant mechanism behind edge cracking.

Keywords Dual-Phase (DP) steels · Edge ductility · Edge cracking · Blanking · Shear-Affected Zone (SAZ)

Abbreviations

AHSS	Advanced High-Strength Steel
CED	Cross Edge Direction
CP	Complex Phase
DIC	Digital Image Correlation
DP	Dual-Phase
EBSD	Electron Backscatter Diffraction
FLC	Forming Limit Curve
GOS	Grain Orientation Spread
HEC	Hole Expansion Capacity
ND	Normal Direction
RD	Rolling Direction
SAZ	Shear-Affected Zone
TD	Transverse Direction

✉ Mahdi Masoumi Khalilabad
m.masoumikhalilabad@utwente.nl

1 Chair of Nonlinear Solid Mechanics, Faculty of Engineering, University of Twente, P.O. Box 217, Enschede 7500 AE, The Netherlands

2 Tata Steel, Research & Development, IJTC, PO Box 10000, IJmuiden 1970 CA, The Netherlands

1 Introduction

There is a high demand for safer cars with higher fuel efficiency for a sustainable future [1]. Advanced high-strength steel (AHSS) grades within automobile frames and body panels offer a solution due to their excellent strength and ductility [2], paving the way to lighter vehicles. Dual-phase (DP) steel is a class of AHSS with attractive properties. However, shear cut edges of DP steel are prone to crack during the forming process. The premature fracture occurs below the prediction of forming limit curves (FLC), which is defined as low edge ductility [3, 4].

The edge ductility issue in dual-phase steels origins from their microstructure [5], which contains hard martensite in a soft ferritic matrix [6]. It means that a significant contrast exists in the mechanical properties of the constituent phases [7]. The microstructure of DP steel is derived from its heat treatment process, which entails controlled cooling from the two-phase region of ferrite and austenite to transform some austenite into ferrite. The remaining austenite is then converted into martensite through rapid cooling. However, there may be small amounts of other phases, including bainite and retained austenite, present in the final product due to the production process. It has been reported that reducing the dif-

ference in hardness [8] or strength [9] between the two phases improves ductility at edges [10]. Moreover, a homogeneous microstructure [11] with a low volume fraction of martensite [4] or lower martensite carbon content [12] leads to better edge performance during forming. Finally, high resistance to edge cracking can be achieved by ferritic-bainitic DP steels or complex phase (CP) steels [13].

Edge ductility is also affected by the edge preparation method. A blanked edge is more susceptible to crack than an edge made by laser-cutting [14], electrical discharge machining (EDM) [4], or abrasive water jet (AWJ) [15]. This premature cracking is related to the shear-affected zone (SAZ) that is created during the cutting process, schematically shown in Fig. 1.

In the shear cutting process, the punch movement pushes the material downward, creating rollover and burnish regions due to plastic deformation. The process continues until a crack initiates, and its propagation separates the material into two parts [16]. As a result, burr and fracture regions of the cut edge are created. The SAZ experiences severe work-hardening and damage accumulation in the form of nucleated voids [17]. The SAZ undergoes further deformation in a forming process, where edge cracks may form. It is worth mentioning that shifting the SAZ toward the scrap side by multi-stage cutting [18, 19] or removing the SAZ by reaming [20] significantly improves the edge ductility. Severe work hardening [21], residual stress [15], roughness [22], damage [23], and nucleated voids [24] of the cut edge have been reported to play a role in edge ductility. The dominant mechanism of edge ductility is not clear yet in the literature.

The shearing/blanking parameters also affect the edge performance during the forming process. The shear cutting parameters mainly consist of the cutting clearance, shearing angle, the cutting tool speed, and tool sharpness. A sharper cutting tool [25] with an optimum range of cutting clearance [26] is beneficial. Inside the optimum range [14, 27], no significant impact from cutting clearance has been observed.
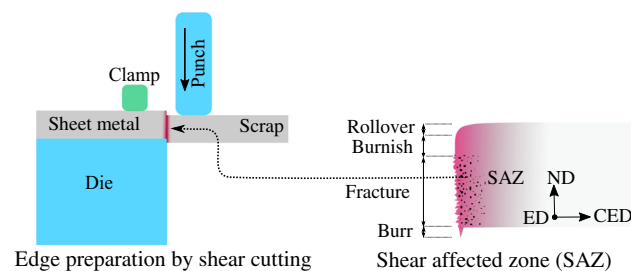
It is essential to indicate the edge performance of the material by a test for the design and optimization of the forming process. The hole expansion capacity (HEC) test based on the ISO16630 standard is commonly used in practice. The test includes a conical tool that expands a punched hole until the operator detects a through thickness crack. Unfortunately, it has been reported that the test parameters affect the HEC value [28]. This drawback originates from the complex stress state of the material edge due to contact with the tool, which causes friction, contact stresses, and out-of-plane deformation. Thus, the sample positioning (burr up or down) [22, 29] or punch design [30] for the same material yields different results. In summary, the HEC value does not solely represent the material's properties.

Several alternatives to the HEC test have been proposed in the literature, including the sheared edge tensile test [31, 32], open hole tensile test [33], side bending test [34], and in-plane bending test [35]. Among these tests, the in-plane bending test is particularly advantageous since it allows for both global examination of edge performance via a moment-curvature diagram and local evaluation via digital image correlation. Furthermore, this test overcomes the limitations of the HEC test, as there is no forming punch in direct contact with the material edge, which eliminates factors such as friction, contact stress, and out-of-plane deformation that can affect the HEC test results.

Although research has been conducted on the factors that contribute to edge ductility, a clear understanding of the primary mechanism responsible is still lacking in the literature. To address this gap, the present study aims to identify the root cause behind edge cracking. To achieve this, the cut edge was subjected to an in-plane bending test setup [36] following shear cutting of the material. The edge was characterized both in its original, as-cut condition, as well as after the in-plane bending test, in its as-bent condition.

CT scanning has been widely used to inspect internal components in various fields [37]. In the current study, it is being employed as a non-destructive method to investigate the evolution of edge cracks. Also, various microscopy techniques were employed at each deformation stage to track the evolution of the edge and distinguish the different mechanisms responsible for edge cracking.

2 In-plane bending test

The in-plane bending test, schematically shown in Fig. 2(a), was used to investigate the edge ductility. The setup was installed on a Zwick tensile machine of 5.0 kN capacity, run at 10 mm min^{-1} cross head speed. To ensure repeatability, each test was repeated at least 4 times.

Dual-phase steel (DP800) from Tata Steel, with a thickness of 1.32 mm, was used in the current study. The chemical

Fig. 1 Schematic of the shear cutting process and the shear-affected zone (SAZ) containing rollover, burnish, fracture, and burr regions. ED, CED, and ND represent edge, cross edge, and normal directions

Fig. 2 The in-plane bending test; a) Fixture and b) Sample geometry with angles for calculating the moment-curvature diagram

(a)   (b)
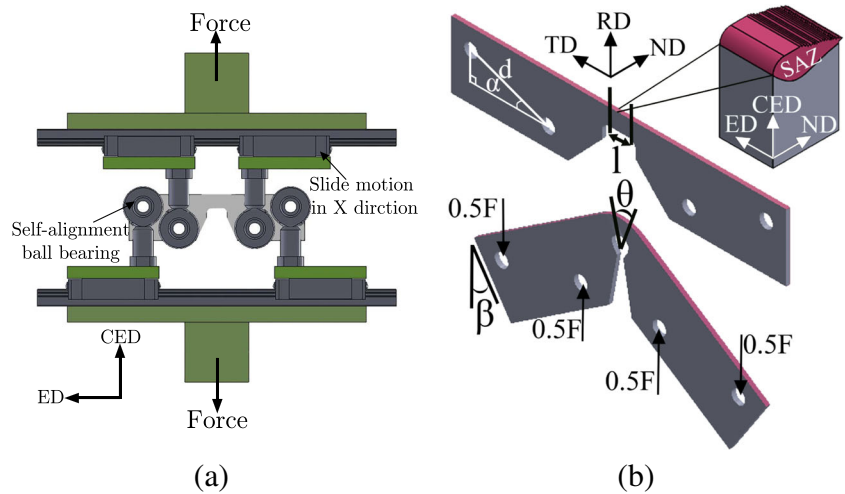
composition (wt%) and mechanical properties in the rolling direction of the steel are presented in Tables 1 and 2, respectively. The top edge of the samples was made by shear cutting for edge ductility investigation. A cutting clearance of 15% with cutting angle of 1.5° was chosen. The rest of the geometry was created by laser cutting as shown in Fig. 2.

The moment-curvature diagram is a proper representation of material behavior during bending. The applied moment to the beam section was calculated by $M = 0.5Fd\cos(\alpha - \beta)$; where F is the measured force by the tensile machine, the parameters d and α are constants associated with the position of the holes on the bending sample as shown in Fig. 2. Parameter β is the rotation angle of sample during bending. The curvature was calculated by $\kappa_{\text{beam}} = \theta/l$; where θ and l are the angle and distance between two imaginary lines in the beam area. Angles β and θ were measured by image analysis using the GOM-Correlate program.

Strain distribution during the in-plane bending test was measured using the digital image correlation (DIC). DIC often uses a white painted background with black speckles on the sample surface for the best contrast. However, the coating makes crack detection harder; therefore, a black pattern was sprayed directly on the material surface without a white background. A sequence of photos was recorded using an IDS camera, model UI-35910CP-C-HQ-R2, and a RICOH lens, model FL-BC7528-9 M. The frame rate of 10 fps was chosen, with a resolution of 4912×3684 pixels. Image analysis was carried out using the open-source Matlab program named Ncorr [38].

3 Microscopic investigation

The edge of the material was deformed in two separate stages in different directions. In the first stage, the deformation is in the normal direction (ND) for edge creation by the shear cutting process. Then, the material edge was deformed further in the edge direction (ED) by in-plane bending, representing the forming process. The amount of damage and microstructural evolution in each deformation stage are investigated. Various microscopy techniques and sample preparations were used at different locations, consisting of the rollover, burnish, fracture, and burr regions.

3.1 Sample preparation for microscopic investigation

The as-cut and as-bent samples were cut by an abrasive cutting machine, model Struers Secotom 60, for microscopy investigation. Subsequently, Bakelite was used for embedding. Then, metallographic samples were ground down with 500 to 2000 grit SiC paper, followed by polishing with 3 to 1 µm diamond suspensions. Finally, ultrasonic cleaning for 5 min removed the residue from the surface. The samples were etched with 4% Nital solution for 7 s to get sufficient contrast between ferrite and martensite. Three different locations near the edge at the top, middle, and bottom of the sheet in thickness direction were selected for void analysis, as shown in Fig. 3a.
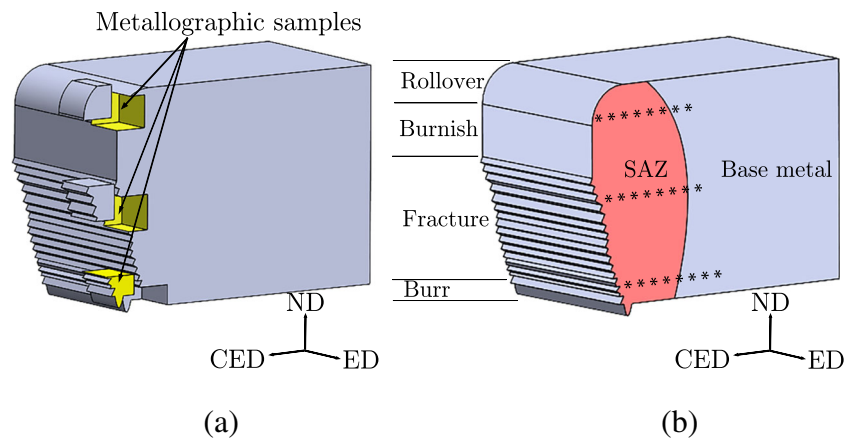
Table 1 The chemical composition (wt%) of steel grade DP800

C	Mn	Si	Cr	Fe and Residuals
0.15	2.06	0.10	0.19	Rest

Table 2 The mechanical properties of the steel grade DP800

R_p (MPa)	R_m (MPa)	A_g (%)	A_{80} (%)
454 ± 4	781 ± 2	14.4 ± 0.2	21.8 ± 0.7

Fig. 3 The edge microscopy investigation; **a** Locations for void analysis, and **b** Spots, indicated by a star sign, selected for EBSD analysis

(a)

(b)

3.2 Microhardness and roughness measurement

The microhardness measurement was done with Leco LM 100AT Hardness Tester. The microhardness map in the CED-ND plane was constructed based on 1155 indentations. The indentation should be far enough from the previously indented locations and edges to avoid measurement errors based on ASTM E384. A safe distance of 50 μm between indents and $50 \mu m$ (i.e., 500 mN) force was considered for measurements. At this force the typical size of the indent is approximately 16 μm. The hardness measurements were taken three times from different cross sections. Finally, a non-contact 3D Optical Profiler (Sensofar S Neox) was used for height and roughness measurement. The area scanned was 1.75 mm × 1.32 mm, with a pixel size of 1.29 μm/pixel. The Z scan was 400 μm, and a magnification of 10x was used.

3.3 Electron backscatter diffraction (EBSD) analysis

The average misorientation angles to the grain mean orientation is called grain orientation spread (GOS), which can be obtained from EBSD analysis and correlates very well with plastic deformation [39]. The EBSD analyses were carried out on a 22 μm×29 μm square region to investigate the evolution of deformation from the shear cut edge toward the bulk of the material, shown schematically in Fig. 3b. The EBSD measurements were collected by a field emission scanning electron microscope, model Jeol-SEM 7200F, operating at 15 kV accelerating voltage with a 70° tilting angle. The electron backscatter patterns (EBSP) were acquired at a step size of 30 nm with a 736×1024 pixel resolution EBSD detector and acquisition system (HKLNordlys, Oxford Instruments plc, UK). Subsequently, the indexed data (pixels with an orientation and phase ID) was post-processed by the MTEX open-source MATLAB toolbox to calculate GOS. Finally, the weighted average value of GOS was determined by using

equation Eq. (1) to compare the plastic deformation of different locations quantitatively,

$$GOS_{mean} = \frac{\sum_{i=1}^{n} W_i x_i}{\sum_{i=1}^{n} W_i} \tag{1}$$

4 Result and discussions

The following sections first cover where the edge cracks initiate and how they propagate. Then, the edge in the as-cut condition is investigated to address the mechanisms that trigger the edge crack initiation during the in-plane bending test.

4.1 Edge crack formation during in-plane bending test

The in-plane bending test creates a moment at the rectangular beam at the center of the sample. Therefore, the shear cut edge, located at the top of the beam, is loaded under tension. Figure 4 shows the strain distribution during the in-plane bending test, recorded by DIC. An edge crack always appears at the top edge due to tensile stress. An advantage of the in-
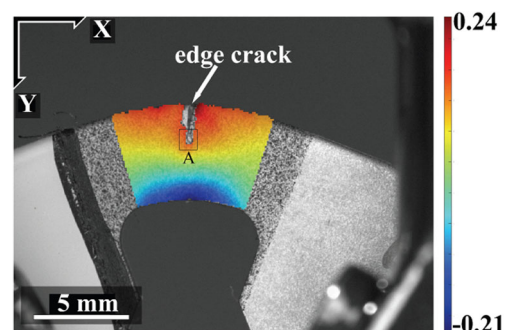
Fig. 4 Maximum principal strain distribution during the in-plane bending test at the CED-ED plane (sheet surface). The top edge is under tension

Fig. 5 Edge crack at ED-CED plane; a) Higher magnification of rectangle A in Fig. 4, b) Higher magnification of rectangle B, and c) Higher magnification of rectangle C. The images are in the CED-ED plane

(a)　　　　　(b)　　　　　(c)
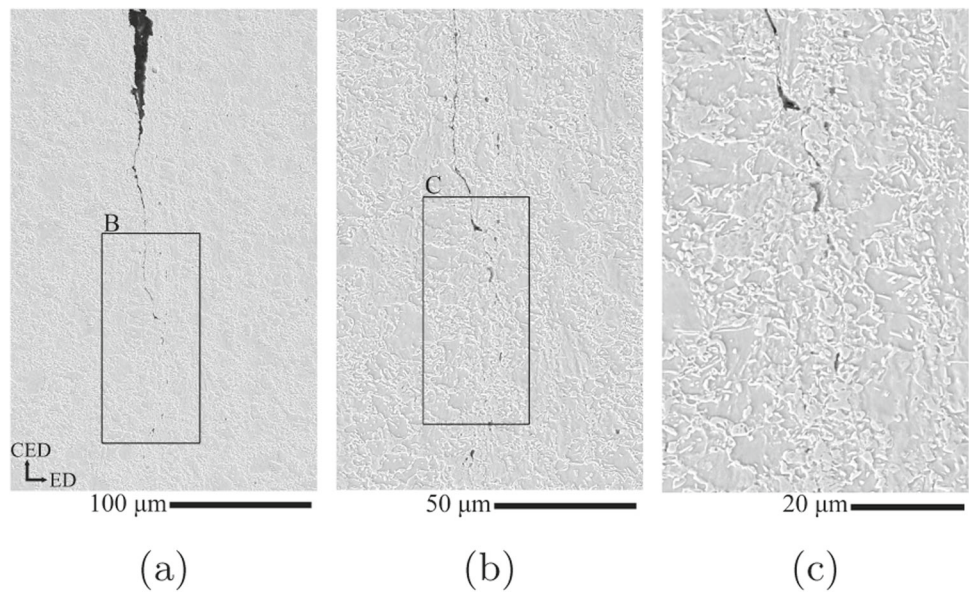
plane bending test is that an edge crack propagates slowly, making tracking of the edge crack easier. Figure 5 shows the high magnification of the edge crack tip in the propagation stage. The void nucleation and coalesced voids are visible

Fig. 6 Edge appearance after in-plane bending test; a) Both fracture surfaces due to the shear cutting and edge cracking are visible, b) Higher magnification of the rectangle B on shear cut fracture surface, c) Higher magnification of rectangle C, d) Higher magnification of rectangle D

(a)　　　　　(b)

(c)　　　　　(d)
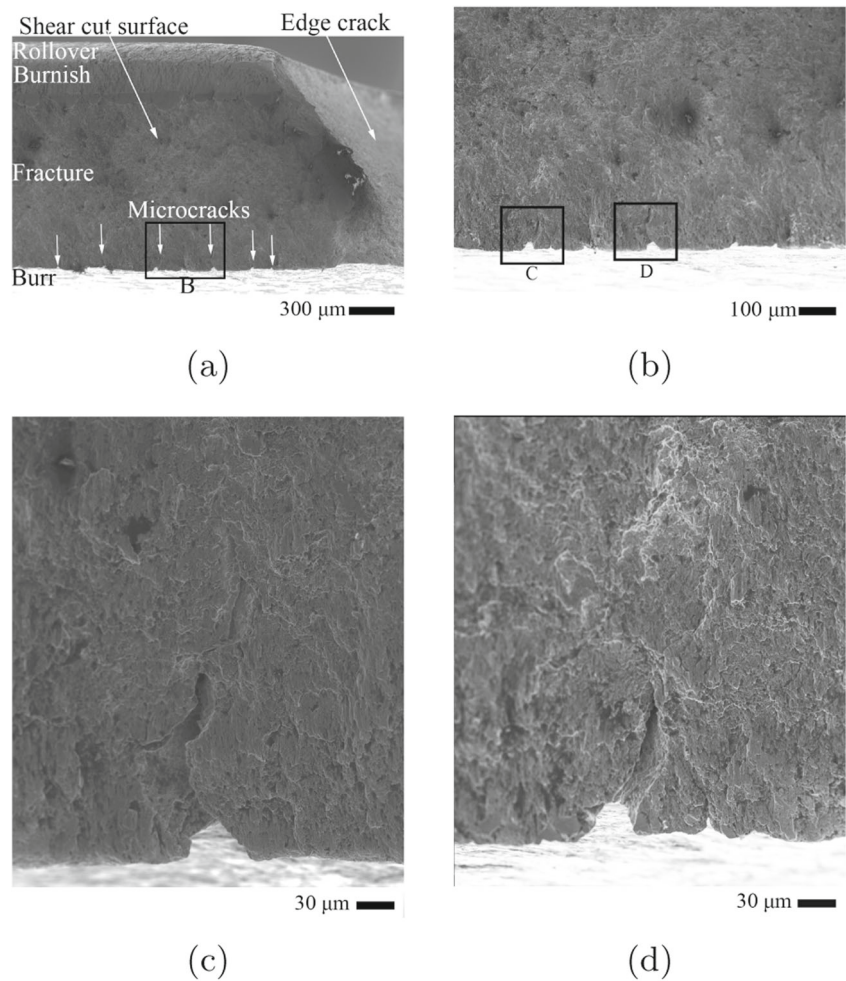
toward the main crack. The initiation of the edge cracks in thickness direction in SAZ region is covered in the following sections by microscopy analysis.

4.1.1 As-bent sample fractography

Both fracture surfaces created by the shear cutting and edge crack are visible in the picture of the as-bent sample in Fig. 6(a). Multiple micro-cracks are visible close to the burr region, while the rollover region is free of micro-cracks, as shown in higher magnification in Fig. 6(b) to (d). Note that based on ISO16630 standard, a crack is defined as an edge crack if it passes the entire thickness of the sample. There-

fore, none of these micro-cracks can be considered as an edge crack. The edge crack fracture surface is presented in Fig. 7(a). Higher magnification from different surface regions in Fig. 7b to d show a ductile fracture as indicated by to the presence of dimples.

4.1.2 Interrupted in-plane bending test

Interrupted bending tests at different strain levels were performed to determine how the micro-cracks evolve into an edge crack during deformation. The interrupted bending tests as presented in Fig. 8 show that the micro-cracks are visible at around 12% of elongation of the edge (major strain). A μCT

Fig. 7 Edge crack appearance after the in-plane bending test; a) Both fracture surfaces due to the shear cutting and edge cracking are visible, b) Higher magnification of the rectangles B, c) Higher magnification of the rectangles C, and d) Higher magnification of the rectangles D
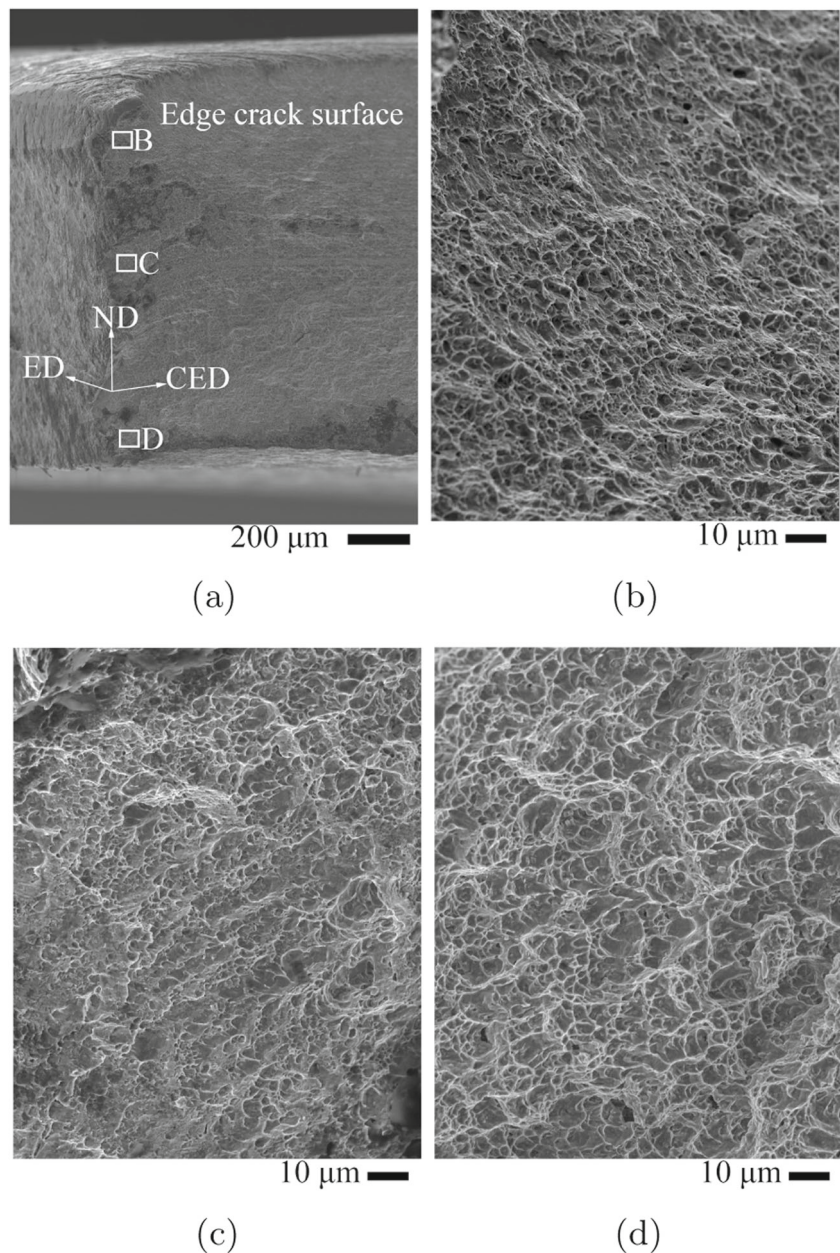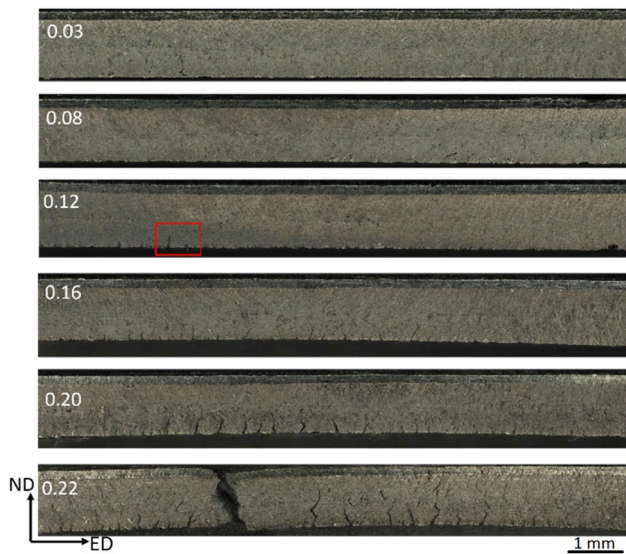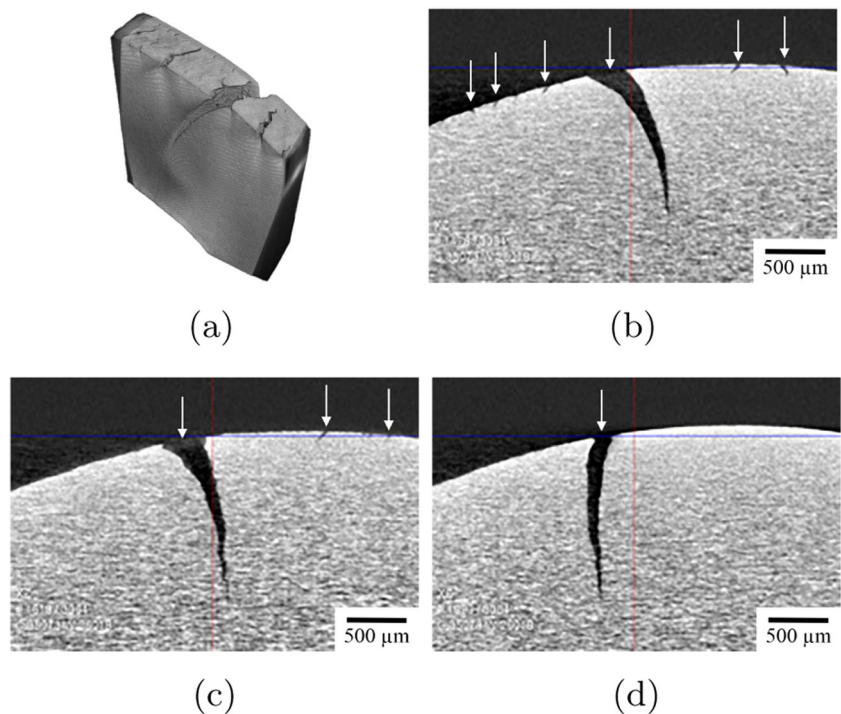
Fig. 8 Edge appearance of DP800 in ED-ND plane during interrupted bending tests at edge strain of 0.03, 0.08, 0.12, 0.16, 0.2 and 0.22

scan as presented in Fig. 9 shows that these micro-cracks are shallow and do not grow in depth, i.e. cross edge direction (CED), before passing the material thickness completely. The micro-cracks increase in number and grow during the in-plane bending test towards the rollover side as the deformation continues. Once they entirely pass the thickness of the material (fracture strain≈0.22), they are identified as edge cracks and start to grow in depth. In summary, the burr region shows more susceptibility to crack initiation than the rollover

region of the shear cut edge. The following sections explain the mechanism behind crack initiation at the burr side.

4.2 Initial state of edge before in-plane bending test

The previous section showed that edge crack preferably initiates in the burr rather than the rollover region. It indicates that the shear cutting process before the bending stage has created inhomogeneous properties over the thickness. The following sections aim to explain the mechanism behind this phenomenon by investigating the as-cut sample, as initial surface after the shear cutting process.

4.2.1 Fracture surface of the as-cut sample

The rollover, burnish, and fracture regions are apparent in Fig. 10A. The rollover and burnish regions are smooth and shiny. The fracture and burr regions are relatively rough. Some extrusions and intrusions on the surface at the burr region are visible with the help of higher magnification in Fig. 10(b). These extrusions and intrusions caused the highest roughness in this location, as shown in Fig. 10b. These irregularities can be a preferred location for edge crack initiation.
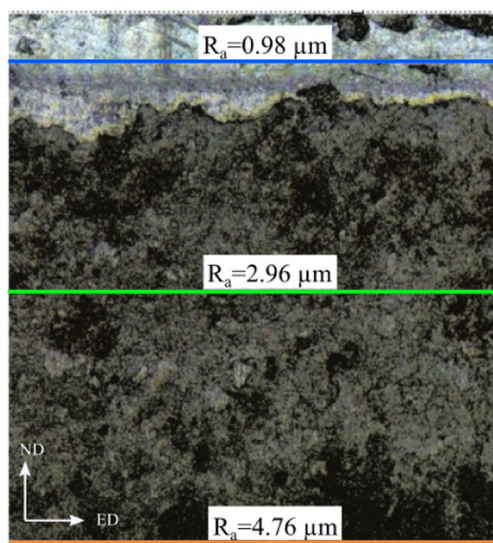
4.2.2 Microstructure evolution

The microstructure of the undeformed material before cutting in the mid-thickness can be seen in Fig. 12. The constructed

Fig. 9 CT scan of DP800 after bending test; a) 3D CT scan, CED-ED plane in b) Burr region c) Mid-thickness. d) Rollover region. Arrows indicate the cracks

Fig. 10 Fracture appearance in as-cut condition; a) Material surface at ED-ND plane and, b) Higher magnification from rectangle B. Multiple intrusions and extrusions in the burr region are visible

(a)

(b)
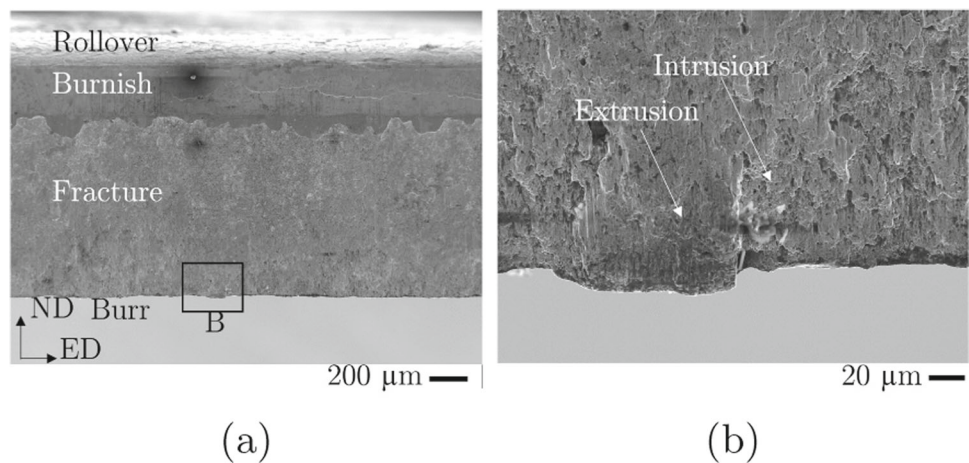
3D image is made from three separate cross-sections in different material orientations. The martensite phase is lighter, while the ferrite is darker. It can be observed that banded martensite is formed in TD and RD due to microsegregation, originating from the casting process [40].

The cutting process deforms the banded microstructure with the material flow. Elongated grains are evident in the ND-CED plane of the as-cut sample in Fig. 13. A critical observation is that no voids are present in rollover and burnish regions (Fig. 13(a)). However, the material edge in fracture and burr regions contains many voids (Fig. 13(b) and (c)), especially in the first 40 μm of the edge. Different mechanisms for void nucleation were observed. The majority of voids are a result of martensite cracking and separation of ferrite–martensite interfaces (Fig. 14(a)). The minority of voids are due to fracture of inclusions and their boundary separation from the matrix (Fig. 14(b) to (c)).
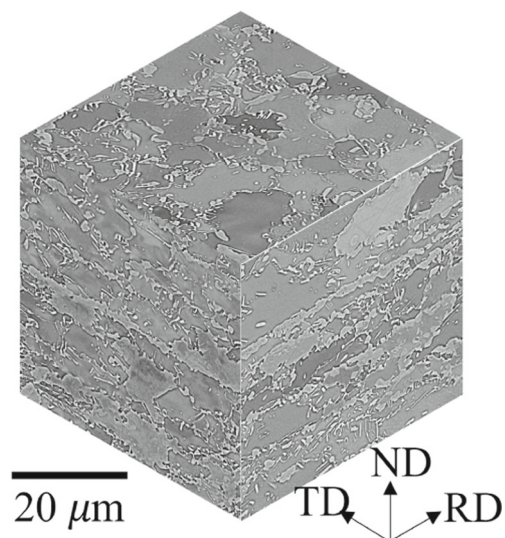
The shear cut edge creates an inhomgouns distribution of voids over the thickness. Then, the in-plane bending test deforms further the shear cut edge. Figure 15 shows the as-bent micrograph in different areas of the material edge. Further deformation during the in-plane bending test did not activate the void nucleation mechanism in rollover and burnish regions (Fig. 15(a)). However, many voids are present in Fig. 15(b) and (c) close to the material edge in the fracture and burr regions. Furthermore, micro-cracks that did not pass the entire thickness of the sheet can be seen in the fracture and burr regions.

4.2.3 Hardness measurement of an as-cut sample

The hardness of material directly correlates with plastic deformation via work hardening. The measured microhardness map of the as-cut sample, overlayed on the edge cross

Fig. 11 Roughness measurement at the top, middle, and bottom of thickness in ED-ND plane of the as-cut sample


Fig. 12 Microstructure of DP800 at the mid-thickness. Martensitic bands are evident in the transverse and rolling directions
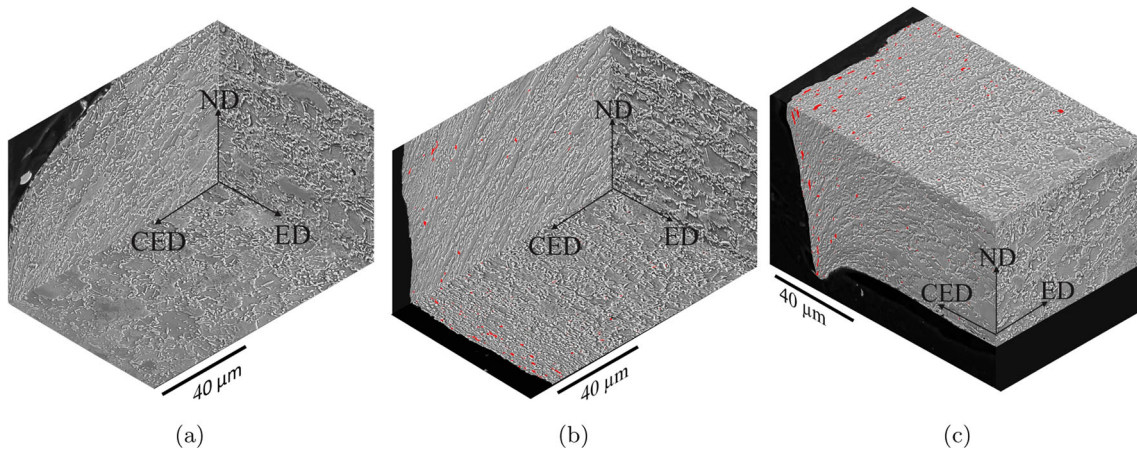
Fig. 13 As-cut sample; a) Rollover and burnish regions, b) Fracture region, c) Fracture and burr regions. The locations for metallography samples can be seen in Fig. 3(a). The voids are indicated by red color

Fig. 14 Damage mechanism of DP800; a) Separation of ferrite/martensite boundaries and fracture of martensite, b) Fracture and separation of inclusions boundary from the matrix, c) EDS maps for Fe and, d) EDS maps for Ti
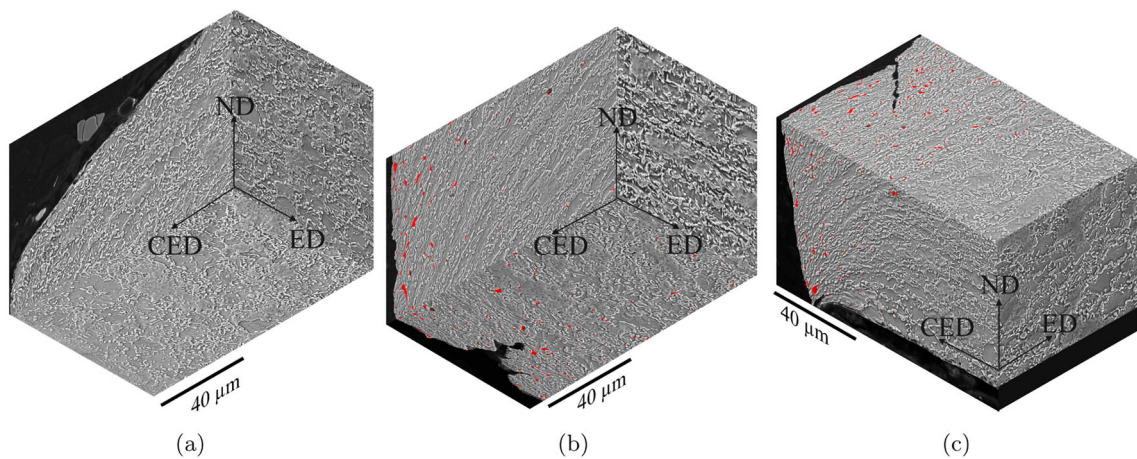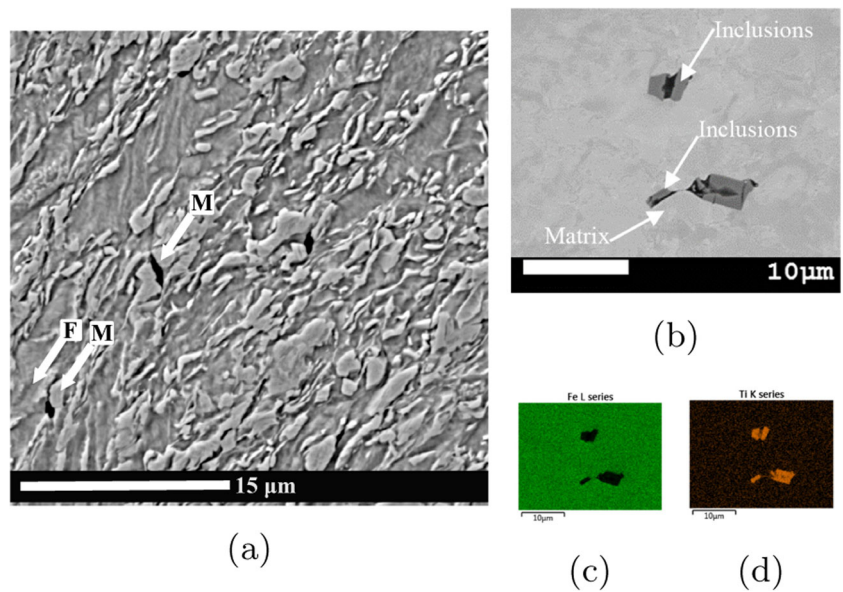
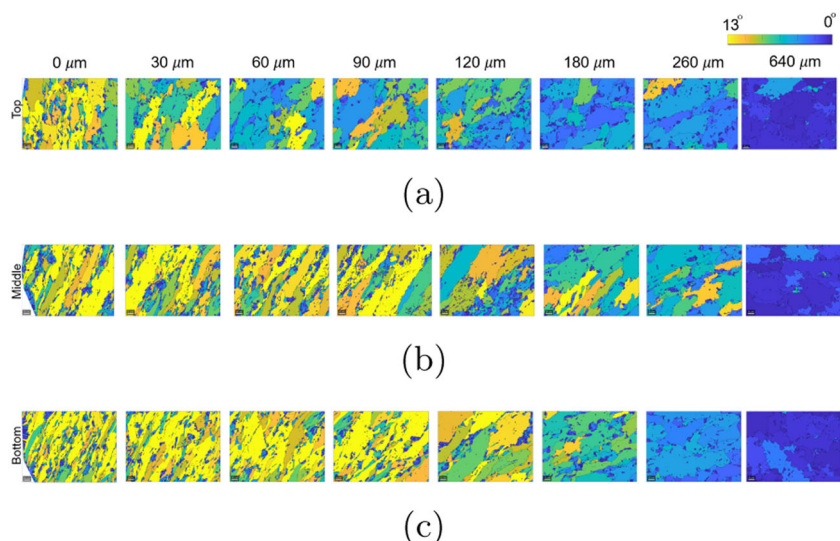**Fig. 15** As-bent sample; **a** Rollover and burnish regions; **b** Fracture region **c** Burr and fracture regions
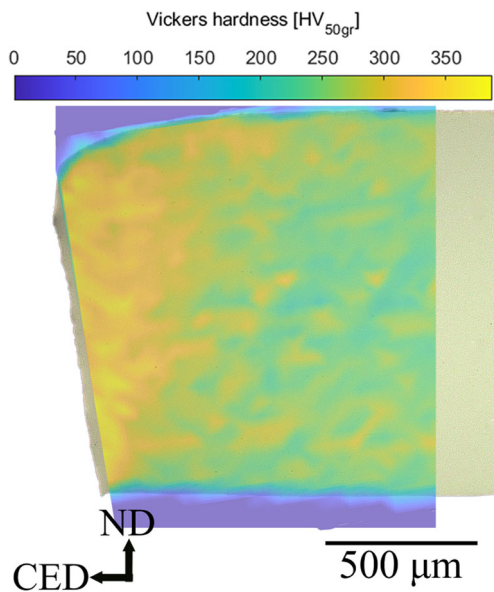
Fig. 16 Overlay of the hardness map onto the edge macrograph in the ND-CED plane for the as-cut sample

Fig. 18 GOS$_{mean}$ vs. distance from the edge after shear cutting as indicator for plastic deformation

section (ND-CED plane), is reported in Fig. 16. Hardness at the edge is maximum, as expected. Performing microhardness tests in a relatively big area provided the global shape of SAZ, and it shows that the maximum size of the affected area is less than 500 μm. EBSD technique is employed in the following sections to reveal the plastic deformation locally at the material edge, which is not feasible with mircrohardenss test due to required safe distance from the edge.

4.2.4 EBSD measurement of an as-cut sample

The evolution of GOS with the distance from the sheared cut edge at three different locations is presented in Fig. 17.

The GOS values increase close to the edge of the material. The SAZ is smaller on the top side, close to the rollover and burnish regions. The rotation of grains toward material flow is also evident, while the grains remain more equiaxed far from the material edge. The calculated GOS$_{mean}$, based on Sect. 3.3 on a 22 μm × 29 μm square region, is reported in Fig. 18. GOS$_{mean}$ magnitudes in mid-thickness and at the bottom are higher than the top edge. In summary, the EBSD result indicates that the top surface (rollover and burnish regions) is less plastically deformed than the rest of the edge; which is in agreement with the volume fraction of voids observed in section 4.2.2.

4.3 Primary mechanism behind edge crack initiation

In previous sections, it was shown that the burr and fracture regions contained more voids than the rollover and burnish regions. Also, these regions were plastically deformed to a greater extent during the cutting process. Finally, the burr region had the highest roughness of all the different areas. Combining these aspects can provide a preferable location for
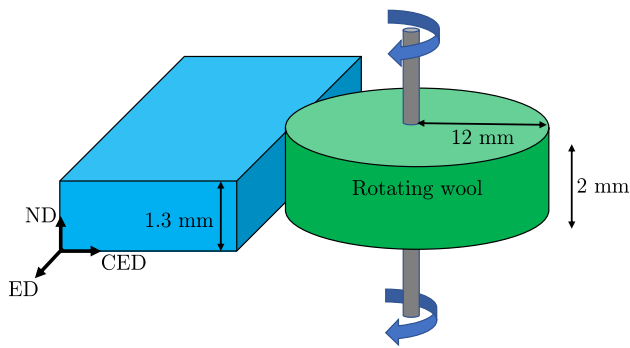
Fig. 17 Evolution of GOS with distance from the sheared cut edge at three locations; **a** 200 μm from the top surface. **b** Mid-thickness, and **c** 200 μm from the bottom surface

Fig. 19 Schematic of the edge polishing process

edge crack initiation in the burr region during the subsequent bending test. However, which mechanism plays a dominant role in edge crack initiation is unclear. The following section aims to distinguish these factors from each other.
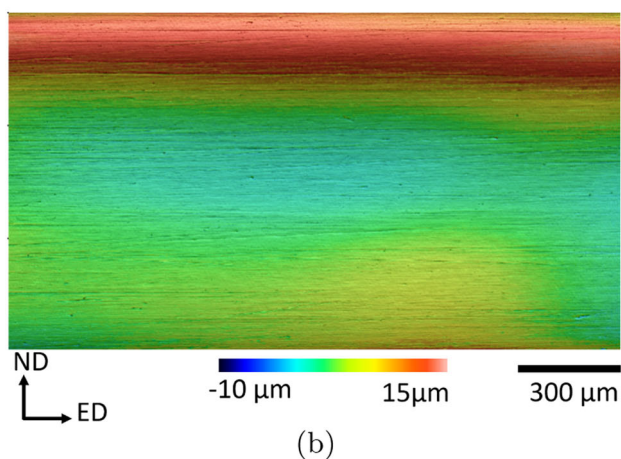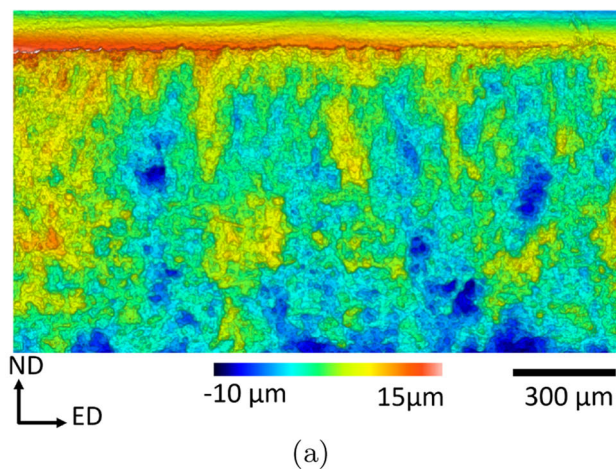

(a)

(b)

Fig. 20 Height profile of the edge surface in ED-ND; **a** As-cut sample and **b** As-polished sample

4.3.1 Edge polishing

Roughness is formed due to geometrical irregularities in the extent of less than 10 μm of the as-cut surface (Fig. 11). Further away from the edge, the first 40 μm of the edge contains the maximum void density (Fig. 13). Finally, the complete SAZ extends to less than 500 μm, as shown in Fig. 16. Since, polishing removes material, it can be used to distinguish the effect of roughness, voids, and plastic deformation on edge ductility. Therefore, samples with varying extend of polishing 10, 40, and 500 μm in the cross edge direction (CED), were compared in the bending test vs. non-polished (as-cut) samples.

4.3.2 Sample preparation

It is essential to have a controlled process that uniformly removes material from the edges, considering that the edge surface is not flat. Figure 19 illustrates the use of a Dremel tool equipped with a rotating wool wheel (12 mm radius and 2 mm thickness) to apply an abrasive paste starting from 6 μm particle size and subsequently decreasing it to 0.25 μm. The rotating wool was chosen to be thicker than the material to ensure it covers the entire thickness and uniformly removes material from the edge. The amount of material removal was controlled under a light microscope at 200× magnification with respect to the distance between the material edge and a reference point far from the edge. The polishing process provided a uniform roughness (Ra=0.2 μm) while preserving the shape of the edge, as shown in Fig. 20. It can be seen that the burnish region is the highest in both samples.

4.3.3 Verification of the polishing process

The microhardness test at the CED was performed to verify that the polishing process was completed as intended in Section 4.3.1. Figure 21 confirms that the SAZ is fully removed
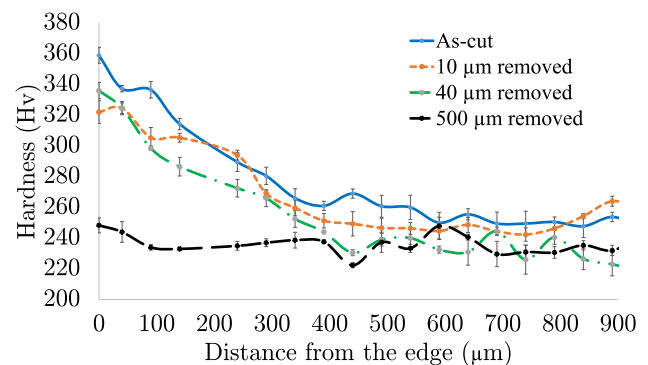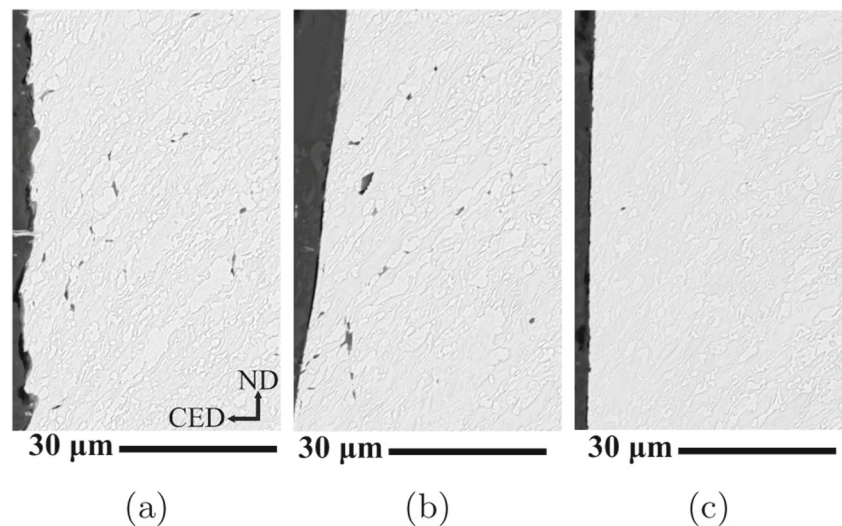

Fig. 21 Microhardness in CED from the edge of as-cut and polished samples
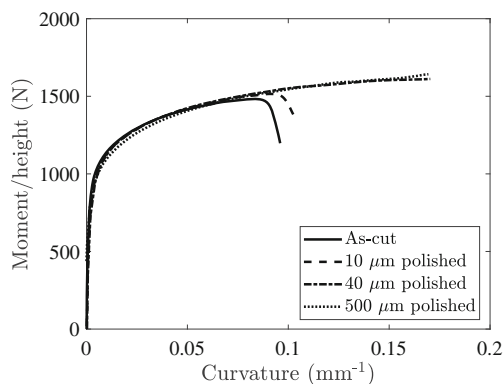
Fig. 22 SEM image in the CED-ND plane of a) as-cut, b) 10 μm polished, and c) 40 μm polished samples. The images were taken from the middle of the thickness at the edge

in the 500 μm polished samples, while SAZ is present in the rest of the samples. Microscopy investigation shows that removing 10 μm of the as-cut sample (Fig. 22(a)) smoothed the rough edge (Fig. 22(b)), while the layer of voids and the rotated grains are still present. Further materiel removal to 40 μm in Fig. 22(c) only eliminated the voids and roughness while keeping the deformed grains and SAZ at the edge of the material. It confirms that the polishing process was performed as intended.

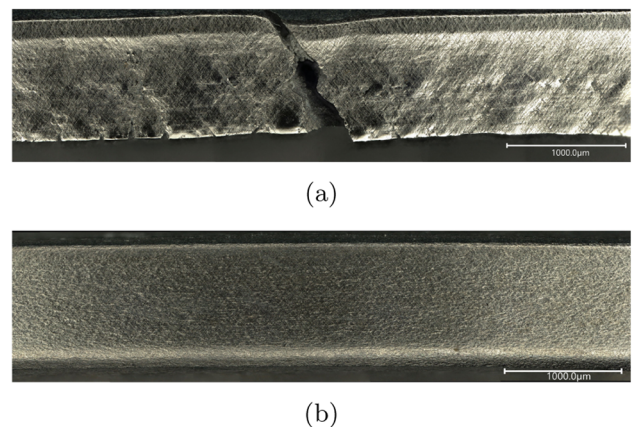### 4.3.4 In-plane bending test on polished samples

The bending test on polished and as-cut (non-polished samples) was used to determine the dominant mechanism behind edge cracking. The as-cut sample broke in the early deformation stage during the subsequent in-plane bending test at fracture strain of 0.22 ± 0.02. The smoothed samples (10 μm polished) also failed, but at a slightly higher strain (0.25 ± 0.02) than the as-cut samples, as shown in the

moment-curvature diagram of Fig. 23. It can be concluded that the roughness has a very small effect on edge ductility.

The samples without initial voids (40 μm polished) did not fail until the maximum achieved deformation of the test. The edge experienced around twice more stretch (true strain=0.42 ± 0.02) than the as-cut sample. The edge is still free of any microcrack, even in the burr region as shown in Fig. 24, and this is a significant improvement. Therefore, the first 40 μm of the cut edge has the most critical influence on edge ducility. This region has voids and the highest values of hardness. These results give a strong indication that voids play the most important role in edge cracking. Combined with high hardness around them, they promote crack nucleation. Hardness, however by itself does not seem to form cracks. This can be justified by the huge jump in fracture strain from 10 μm to 40 μm polishing. If hardness was the main factor, a more gradual change would be expected; since there is still hard material in the remaining portion of the edge.

Fig. 23 The moment-curvature diagram during the in-plane bending test for the as-cut sample with and without polishing

Fig. 24 Edge appearance of 10 μm and 40 μm polished samples in ED-ND plane after bending test

Fig. 25 The cross-section of 500 μm polished sample in CED-ND; a) Before bending test and b) After bending test

(a) (b)
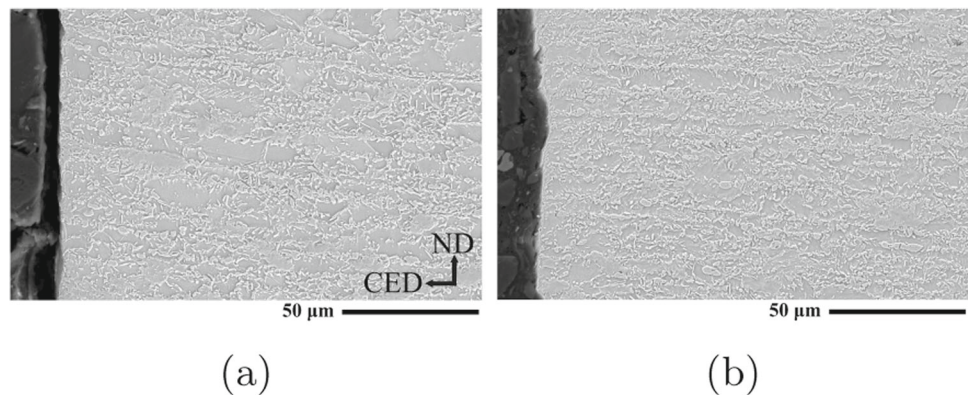
By removing 500 μm from the edge all effects from shear cutting are eliminated, leaving only the base metal, as shown in Fig. 25(a). Therefore, it can be considered a reference edge. The 500 μm polished sample did not fail during the in-plane bending test. The edge of the reference sample after the bending test is presented in Fig. 25(b). It demonstrates that the plastic deformation during the in-plane bending test is insufficient for the void nucleation mechanism in a uniaxial stress state close to the edge. At the same time, this plastic deformation is more than enough to grow and coalesce the initial voids produced by cutting in the shear stress state, causing the micro-cracks on the edge of the sample.

5 Conclusions

The edge prepared by shear cutting was investigated to address the low edge ductility in dual-phase steels. A DP800 sheet was shear cut in the first step. Subsequently, the cut edge underwent further deformation during the in-plane bending test. Void distribution and non-uniform plastic deformation were explored with the help of microscopic analysis in different regions of the edge. The main conclusions for the material investigated are listed as follows.

- The edge properties along the thickness direction are inhomogeneous due to the cutting process; further deformation creates many micro-cracks on the burr side while only a few span the entire thickness.
- The shear cutting process induces more plastic deformation and a higher density of voids in the mid-thickness and burr side of the edge than on the rollover side, as indicated by EBSD and SEM analyses.
- The maximum roughness in the burr region combined with high plastic deformation and void volume fraction can trigger crack initiation in the burr region.
- These micro-cracks tend to first pass through the entire thickness. Afterwards, through-thickness cracks grow into the depth of the material.

- The initial void volume fraction inside a severely hardened layer of the as-cut edge plays a more critical role than roughness in edge ductility.
- Removing the volume from edge with high void density is enough to significantly increase the edge ductility. It is not necessary to remove the complete shear-affected zone.

Declarations

References

1. Badji R, Cheniti B, Kahloun C et al (2021) Microstructure, mechanical behavior, and crystallographic texture in a hot forged dual-phase stainless steel. The International Journal of Advanced Manufacturing Technology 116(3):1115–1132

2. Kong Z, Zhang J, Li H et al (2018) Deep drawing and bulging forming limit of dual-phase steel under different mechanical properties. The International Journal of Advanced Manufacturing Technology 97(5):2111–2124

3. de Oliveira AR, Lajarin SF, Rebeyca CJ et al (2022) Influence of drawbead geometry and blank holder force on the dual phase steel formability. The International Journal of Advanced Manufacturing Technology 121(9):5823–5833

4. Balisetty V, Chakkingal U, Venugopal S (2021) Evaluation of stretch flangeability of dual-phase steels by hole expansion test. International Journal of Advanced Manufacturing Technology 114(1–2):205–217. https://doi.org/10.1007/s00170-021-06850-9

5. Won C, Lee W, Lee Hy et al (2020) Effect of two-stage press blanking on edge stretchability with third-generation advanced high-strength steels. The International Journal of Advanced Manufacturing Technology 110(1):13–27

6. Basaeri A, Khorsand H, Eslami-Farsani R et al (2020) Comparative experimental and numerical study on the mechanical properties, formability, and microstructure of two high strength steel sheets. The International Journal of Advanced Manufacturing Technology 108(7):2023–2033

7. Barnwal VK, Lee SY, Choi J et al (2020) Fracture assessment in dual phase and transformation-induced plasticity steels during 3-point bending. Theoretical and Applied Fracture Mechanics 110(102):834. https://doi.org/10.1016/j.tafmec.2020.102834

8. Takashima K, Hasegawa K, Toji Y et al (2017) Void generation in cold-rolled dual-phase steel sheet having excellent stretch flange formability. The Iron and Steel Institute of Japan 57(7):1289–1294

9. Mukherjee M, Tiwari S, Bhattacharya B (2018) Evaluation of factors affecting the edge formability of two hot rolled multiphase steels. International Journal of Minerals, Metallurgy and Materials 25(2):199–215. https://doi.org/10.1007/s12613-018-1563-1

10. Pan L, Xiong J, Zuo Z et al (2020) Study of the stretch-flangeability improvement of dual phase steel. Procedia Manufacturing 50(2019):761–764. https://doi.org/10.1016/j.promfg.2020.08.137

11. Terrazas OR, Findley KO, Van Tyne CJ (2017) Influence of martensite morphology on sheared-edge formability of dual-phase steels. ISIJ International 57(5):937–944. https://doi.org/10.2355/isijinternational.ISIJINT-2016-602

12. Madrid M, Tyne CJV, Sriram S, et al (2018) Hole expansion ratio in intercritically annealed QP 980 / 1180 steel grades as a function of testing condition. IOP Conference Series: Materials Science and Engineering 418(1):012,083. https://doi.org/10.1088/1757-899X/418/1/012083

13. Pathak N, Butcher C, Adrien J et al (2020) Micromechanical modelling of edge failure in 800 MPa advanced high strength steels. Journal of the Mechanics and Physics of Solids 137. https://doi.org/10.1016/j.jmps.2019.103855

14. Hoefnagels JP, Du C, Tasan C (2020) Laser-induced toughening inhibits cut-edge failure in multi-phase steel. Scripta Materialia 177:79–85. https://doi.org/10.1016/j.scriptamat.2019.09.022

15. Behrens BA, Diaz-Infante D, Altan T et al (2018) Improving hole expansion ratio by parameter adjustment in abrasive water jet operations for dp800. SAE International Journal of Materials and Manufacturing 11(3):241–252

16. Otroshi M, Meschut G (2022) Influence of cutting clearance and punch geometry on the stress state in small punch test. Eng Fail Anal 136(106):183. https://doi.org/10.1016/J.ENGFAILANAL.2022.106183

17. Chang Y, Han S, Li X, et al (2018) Effects of different cutting processes on characteristics of cut damage for the third-generation automobile medium-mn steel. Steel Research International 89(9):1700,375. https://doi.org/10.1002/srin.201700375

18. Kurniawan Y, Mahardika M, S, et al (2018) Maximizing the Expansion Ratio through Multi-stage Shear-cutting Process during Collar Forming. In: IOP Conference Series: Materials Science and Engineering, https://doi.org/10.1088/1757-899X/418/1/012071

19. Paetzold I, Feistle M, Golle R, et al (2018) Determination of the minimum possible damage due to shear cutting using a multi-stage shear cutting process. In: IOP Conference Series: Materials Science and Engineering, https://doi.org/10.1088/1757-899X/418/1/012070

20. Feistle M, Golle R, Volk W (2022). Edge crack test methods for AHSS steel grades: A review and comparisons. https://doi.org/10.1016/j.jmatprotec.2021.117488

21. Feistle M, Kindsmüller A, Pätzold I et al (2022) Influence of Sheet Metal Pre-forming on Edge Crack Sensitivity using an AHSS Steel Grade. International Journal of Material Forming 15(4):1–11. https://doi.org/10.1007/s12289-022-01669-5

22. Pathak N, Butcher C, Worswick M (2016) Assessment of the Critical Parameters Influencing the Edge Stretchability of Advanced High-Strength Steel Sheet. Journal of Materials Engineering and Performance 25(11):4919–4932. https://doi.org/10.1007/s11665-016-2316-9

23. Habibi N, Mathi S, Beier T et al (2022) Effects of Microstructural Properties on Damage Evolution and Edge Crack Sensitivity of DP1000 Steels. Crystals 12(6):845. https://doi.org/10.3390/cryst12060845

24. Sun Q, Zan D, Chen J et al (2015) Analysis of edge crack behavior of steel sheet in multi-pass cold rolling based on a shear modified GTN damage model. Theoretical and Applied Fracture Mechanics 80:259–266. https://doi.org/10.1016/j.tafmec.2015.06.003

25. Masoumi Khalilabad M, Perdahcıoğlu ES, Atzema EH et al (2022) An in-plane bending test to characterize edge ductility in high-strength steels. Journal of Materials Engineering and Performance. https://doi.org/10.1007/s11665-022-07202-8

26. Shih HC, Shi MF (2011) An innovative shearing process for ahss edge stretchability improvements. Journal of Manufacturing Science and Engineering 133(6):061,018. https://doi.org/10.1115/1.4005460

27. Levy B, Van Tyne C (2012) Review of the shearing process for sheet steels and its effect on sheared-edge stretching. Journal of materials engineering and performance 21(7):1205–1213

28. Park S, Cho W, Jeong BS et al (2022) A dual-scale fe simulation of hole expansion test considering pre-damage from punching process. International Journal of Solids and Structures 236(111):312

29. Nguyen DT, Tong VC (2021) A numerical and experimental study on the hold-edge conditions and hole-expansion ratio of hole-blanking and hole-expansion tests for ferrite bainite steel (FB590) sheets. Ironmaking and Steelmaking 48(8):986–994. https://doi.org/10.1080/03019233.2020.1849934

30. Paul SK (2020) Effect of punch geometry on hole expansion ratio. Proceedings of the Institution of Mechanical Engineers, Part B: Journal of Engineering Manufacture 234(3):671–676. https://doi.org/10.1177/0954405419863222

31. Atzema E, Seda P (2015) Sheared edge tensile test improved: SETi. Forming Tech Forum, Zurich, Switzerland pp 984–991

32. Wang J, Link TM, Merwin MJ (2011) AHSS edge formability in sheared-edge tension. Proceedings of the International Conference on New Developments in Advanced High-Strength Sheet Steels pp 361–366

33. Feistle M, Pätzold I, Golle R, et al (2019) Open hole tensile tests for the determination of the edge-crack sensitivity of sheared holes dependent on specimen geometry, cutting parameters, and the notch factor. Procedia Manufacturing 29:412–419. https://doi.org/10.1016/j.promfg.2019.02.156, "18th International Conference on Sheet Metal, SHEMET 2019" "New Trends and Developments in Sheet Metal Processing"

34. Matsuno T, Sato K, Okamoto R et al (2016) Synergy effect of shear angle and anisotropic material ductility on hole-expansion ratio of

high-strength steels. Journal of Materials Processing Technology 230:167–176. https://doi.org/10.1016/j.jmatprotec.2015.10.018

35. Masoumi Khalilabad M, Perdahcıoğlu ES, Atzema EH, et al (2022) Measurement of edge fracture strain of dual-phase steels by in-plane bending test. IOP Conference Series: Materials Science and Engineering 1238(1):012,039. https://doi.org/10.1088/1757-899x/1238/1/012039

36. Naseem S, Perdahcloğlu ES, Geijselaers HJ et al (2020) A New in-Plane Bending Test to Determine Flow Curves for Materials with Low Uniform Elongation. Experimental Mechanics. https://doi.org/10.1007/s11340-020-00621-5

37. Gogolin A, Wasilewski M, Ligus G et al (2020) Influence of geometry and surface morphology of the u-tube on the fluid flow in the range of various velocities. Measurement 164(108):094

38. Blaber J, Adair B, Antoniou A (2015) Ncorr: Open-Source 2D Digital Image Correlation Matlab Software. Experimental Mechanics 55(6):1105–1122. https://doi.org/10.1007/s11340-015-0009-1

39. Wu Y, Uusitalo J, DeArdo AJ (2020) Investigation of effects of processing on stretch-flangeability of the ultra-high strength, vanadium-bearing dual-phase steels. Materials Science and Engineering A 797(July):140,094. https://doi.org/10.1016/j.msea.2020.140094

40. Krauss G (2003) Solidification, segregation, and banding in carbon and alloy steels. Metallurgical and Materials Transactions B 34(6):781–792